



---

**Utilizing of ASTER multispectral data in alteration zones and granitic rock types discrimination at Gabal Abu El-Tiyur area, central Eastern Desert, Egypt**

**Yasser Salah Badr and Mahmoud Elsaid**

Nuclear Materials Authority, P.O. Box 530, Maadi, Cairo, Egypt

**Received:** 20 June 2022

**Accepted:** 14 July 2022

**Published:** 20 July 2022

---

**ABSTRACT**

The present work aims at examining the capability of ASTER VNIR-SWIR bands to discriminate the granitic rocks and detection of alteration types within them, which could be a possible hosting for U-mineralization in the arid climate. The applied image processing techniques comprising relative band depth, band ratios, minimum noise fraction and color band composites supervised classification as well as two spectral mapping methods (matched filtering and mixture tuned matched filtering) were efficient in the granitic rocks discrimination and alteration end-members (hematite, muscovite, kaolinite and chlorite) identification. These results easily differentiate the mélange matrix into a) metasediments rich in blocks and b) metasediments poor in blocks. Also, the granitic rocks are classified into granodiorite, monzogranite, syenogranite, alkali-feldspar granite and alkaline (riebeckite) granite. The associated abnormal level of radioactivity exhibits 18 ppm and 31 ppm for eU, eTh respectively and mainly restricted to the alkali-feldspar granites, which significantly have higher hematite and muscovite content rather than the other exposures. A detailed geologic map of scale 1:100,000 is constructed from the interpretation of the processed ASTER images, fieldwork and petrographic studies. The results confirmed the ability of ASTER data and recommended it as a rapid and cost-effective tool in geological and mineralogical mapping in arid climate especially when the processing based on a detailed knowledge of the rock mineral assemblages.

**Keywords:** Gabal Abu El-Tiyur, Relative Band Depth, Band Ratios, Minimum Noise Fraction, Matched Filtering, Mixture Tuned Matched Filtering, geological mapping, radioactivity.

---

**1. Introduction**

The Egyptian Eastern Desert (ED) of Egypt as a part of the Pan-African Arabian - Nubian Shield is covered by igneous and metamorphic rocks that were formed in the East African Orogeny during the collision between East and West Gondwana and the closure of the Mozambique Ocean 600 Ma (Stern, 1994 and Kusky and Matsah, 2003). The ED is traditionally divided into three subdivisions (northern (NED), central (CED) and southern (SED) divided by two rough lines are running from River Nile to Red Sea) confining parts with common geographic and lithostructural discontinuities (Stern, 1979 and Abdel Meguid, 1992). The Central Eastern Desert (CED) is generally built up of ophiolitic mélange and their associated rocks together with subordinate molasse-type sediments and late-tectonic volcanics (El Ramly *et al.*, 1993). The granitoids intrusive rocks covering about 60% of the total basement ground of the Nubian Shield in Egypt (Stern and Hedge, 1985). These rocks have attracted the attention of Nuclear Materials Authority (NMA) staff since the discovery of some U-mineralization, which mainly related to the post-collision granites in the ED of Egypt; e.g., G. El-Erediya (El-Kassas, 1974), G. El-Missikat (Bakhit, 1978), and G. Gattar (Salman *et al.*, 1990).

Remote sensing has widely used for geological mapping and mineral exploration and their abilities increase with the advanced satellite missions of higher spatial, spectral, radiometric and temporal resolutions (Abrams *et al.*, 1983; Sultan, 1986, Kaufmann, 1988; Vincent, 1997; Clark, 1999).

---

**Corresponding Author:** Yasser Salah Badr, Nuclear Materials Authority, P.O. Box 530, Maadi, Cairo, Egypt.  
E-mail: yasenma82@gmail.com

The Advanced Spaceborne Thermal Emission and Reflection Radiometer (ASTER) is a high spatial, spectral and radiometric resolution multispectral remote sensing instrument that consists of three separate instrument subsystems providing observation in three different spectral regions of the electromagnetic radiation (EMR), including visible and near infrared (VNIR), short wavelength infrared (SWIR) and thermal infrared (TIR) (Table.1). The spectral region between 0.4 to 2.5  $\mu\text{m}$  that includes ASTER-VNIR and SWIR regions shows common absorption bands caused by vibrational processes due to over tones and combination tones of fundamental O-H groups (Hunt and Ashley, 1979).

Iron oxides and hydroxides minerals show charge transfer and  $\text{Fe}^{3+}$  crystal field bands between VNIR wavelength ranges. OH-bearing minerals including clays, sulfates and carbonates exhibit diagnostic spectral absorption features in SWIR regions (2.0 to 2.5 $\mu\text{m}$ ), so this wavelength region is the most descriptive for hydrothermal alteration mineralization related to the over tones and combination tones vibrations of octahedrally coordinated cations (typically Al, Fe, and Mg) bonded with O-H groups (Clark, 1999).

The study area has been regionally mapped before by Sabet, 1961; El Gaby, 1975; Ragab *et al.*, 1993; El-Kalubi, *et al.*, 1995; Meky, 1997; Akaad and Abu El Ela, 2002; Abd El-Wahed *et al.*, 2002; Hegazi and Hamimi, 2002; El-Husseiny, 2003; Fowler *et al.*, 2007; Hassan *et al.*, 2014 and EL-Sherif, 2015. This study gave an understanding to the geology of G. Abu El-Tiyur area during processing of ASTER VNIR-SWIR bands and laboratory investigations to discriminate the granitic rocks (99 $\text{km}^2$  about 34% of the mapped area) and detection of alteration types within them, which could be a possible hosting for U-mineralization.

**Table 1:** Characteristics of ASTER data that used in the study area

Subsystem	Band No.	Spectral range ( $\mu\text{m}$ )	Radiometric resolution (bits)	Spatial resolution (m)
VNIR	1	0.52-0.60	8	15
	2	0.63-0.69		
	3N	0.78-0.86		
	3B	0.78-0.86		
SWIR	4	1.6-1.7	8	30
	5	2.145-2.185		
	6	2.185-2.225		
	7	2.235-2.285		
	8	2.295-2.365		
	9	2.360-2.430		
TIR	10	8.125-8.475	12	90
	11	8.475-8.825		
	12	8.925-9.275		
	13	10.25-10.95		
	14	10.95-11.65		

## 2. Geologic setting

Gabal (G.) Abu El-Tiyur area is located at the central Eastern Desert (CED) of Egypt between latitudes 25° 37' 08" and 25° 47' 58" N and longitudes 34° 12' 35" and 34° 22' 50" E respectively (Fig.1), covering an area about 288  $\text{km}^2$ . It lies about 30 km south of El Quseir city on the Red Sea coast. The area is characterized by a rugged topography with a gradual rise of the terrain westwards. G. Abu El-Tiyur represents the highest elevation point in the study area (about 1110m above sea level). Climatically, the study area is lying within the arid belt, which includes northern Africa and southeastern Asia. Vegetation is scarce and inhabitants are few. The basement rocks in the study area comprising three petro-tectonic assemblages; allochthonous ophiolitic assemblage, arc granitoids and late to post-collision granites. The allochthonous ophiolitic assemblage is including dismembered ophiolitic rocks (metaultramafites - serpentinites and related rocks - and metagabbros blocks and fragments embedded in metasediments).

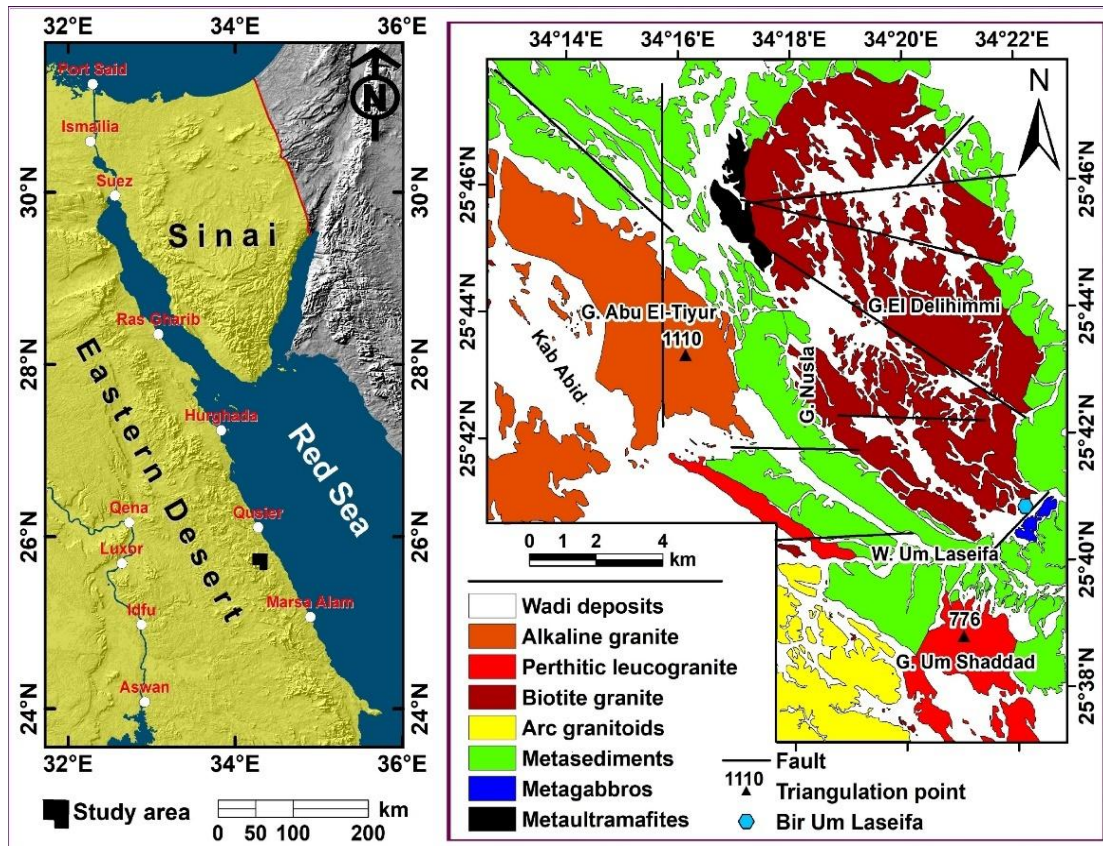


**Fig.1:** Geological map of G. Abu El-Tiyur area (CED), Egypt; modified after Mohamed, 2001 and Hegazi and Hamimi, 2002.

The metaultramafites, comprising serpentinites and related rocks, are cropping out in the northern part of the mapped area as an elongated to lensoidal mass trending NW-SE direction covering 3 km<sup>2</sup>. Serpentinites are fine- to medium-grained, dark green to dark grey color, cavernous, locally sheared and usually altered to talc-carbonates of yellowish-brown color (Fig.2a).

The ophiolitic metagabbros are cropping out in the extreme southeastern part of the mapped area. These rocks are massive, medium- to coarse-grained, greenish grey to dark green in color and have low- to moderate-relief. Metagabbros are partially to completely altered, intensively deformed, foliated and sometimes exhibit minor folds of different styles.

Metasediments (the *mélange* matrix) are cropping out as two major elongated belts trending in NW-SE and WNW-ESE directions covering 56 km<sup>2</sup> and represented mainly by highly sheared and foliated schists and metagraywackes as well as minor masses of polymictic metaconglomerates. Metasediments are low to moderate topography, fine- to very fine-grained and are varying in color due to their various composition. These rocks are well foliated (Fig.2b) and lineated and show minor folds of different styles and trends. The foliation exhibits two main trends NW-SE and NE-SW directions. The processed images of ASTER data differentiated the studied metasediments into two varieties; a) metasediments rich in blocks (Fig.2c) that appear as a semi-circle belt along the northern contact of G. El Delihimmi granites and b) metasediments poor in blocks, which is dominant, well foliated and more abundant than the first one that exposed all over the area.

Arc granitoids (granodiorite) are cropping out in the southern part of the mapped area covering 11 km<sup>2</sup>. They are generally of low topography, massive, medium- to coarse-grained, light to dark grey in color and commonly exfoliated (Fig.2d). These rocks were previously mapped as younger granites (Sabet, 1961 and Ragab *et al.*, 1993) and as older granitoids (Mohamed, 2001, Hegazi and Hamimi, 2002; Fowler *et al.*, 2007 and Hassan *et al.*, 2014).

Late to post-collision granites are the most important rock unit covering about 88 km<sup>2</sup> (about 30%) of the mapped area. These granites represented by G. Abu El-Tiyur, G. Um Shaddad, and El Delihimmi- Nusla granites.

G. Abu El-Tiyur (alkaline (riebeckite) granite) is cropping out in the western part of the mapped area as an elongated pluton with conspicuous peaks trending in NW-SE direction covering 24 km<sup>2</sup>. G. Abu El-Tiyur is medium- to coarse-grained, pink to pinkish buff in color and composed of K-feldspars, quartz, plagioclase, rare amount of mafic minerals and alkali amphibole (mainly riebeckite). The pluton has sharp contacts with the metasediments and exhibit exfoliation weathering. G. Abu El-Tiyur are previously mapped as cataclastic granites by Sabet (1961); as biotite granite, riebeckite granite and alkali-feldspar granite (Meky, 1997 and Hassan *et al.*, 2014); alkali-feldspar granite (Akaad and Abu El Ela, 2002; El-Husseiny, 2003 and Fowler *et al.*, 2007 and as alkaline granite (Hegazi and Hamimi, 2002).

G. Um Shaddad (776 m above sea level.) is located in the southeastern part of the mapped area with limited exposure (about 7 km<sup>2</sup>) as an irregular granitic body trending in E-W direction. This granite is medium- to coarse-grained, pink to reddish pink color and composed essentially of K-feldspars, quartz, plagioclase and rare amount of mafics. It intrudes the surrounding metasediments with sharp intrusive contacts. G. Um Shaddad is compositionally classified as monzogranite and/or syenogranite (Akaad and Abu El Ela, 2002); as perthitic leucogranite (Hegazi and Hamimi, 2002) and as alkali-feldspar granite (El-Husseiny, 2003, Fowler *et al.*, 2007 and Hassan *et al.*, 2014).

El Delihimmi- Nusla granites represent the largest granitic intrusion (covering 46 km<sup>2</sup>) in the study area, showing an oval shaped mass elongated in the NW-SE direction parallel to the Red Sea and exhibit low to moderate relief. These granites have sharp intrusive contacts with the ophiolitic assemblage rocks. Quartz veins and veinlets (Fig.2e) are predominant in these granites and sometimes stained by iron oxides. These granites are altered where kaolinization and hematitization are the dominant alteration types (Fig.2f). Sabet (1961) classified El Delihimmi- Nusla granites as granodiorite and muscovite granite. El Gaby (1975) considered these granites as late- to post-orogenic granite and originated due to magmatic differentiation. Shalaby (1982) classified them into biotite granite and muscovite granite while Akaad and Abu El Ela (2002) and Fowler *et al.*, (2007) mapped them as granodiorite. El-Husseiny (2003) classified these granites as monzogranite and finally Hassan *et al.*, 2014 classified them as alkali-feldspar granite gneissic in parts. The present study differentiated El Delihimmi- Nusla granites into granodiorite, monzogranite and syenogranite at the core of the intrusion while the outer peripheries are mainly alkali-feldspar granite except the south parts of this granitic intrusion.

### 3. Materials and Methods

The ASTER data used in this study is a cloud free level 1B (Radiance at Sensor) scene (ASTL1B 0403290830150707010028), which acquired on July 01, 2007. The scene was pre georeferenced to UTM zone 36-north projection using the WGS84 datum. Cross-Talk Correction was performed to remove the effect arises from dispersion of the incident light of band-4 detector into bands 5 and 9 (Iwasaki and Tonooka, 2005). ASTER VNIR and SWIR bands were resampled to 30m × 30m pixels using the nearest neighbor algorithm to preserve SWIR bands spectral characteristics (Galvão *et al.*, 2005). Atmospheric correction was performed using the Fast Line of Sight Atmospheric Analysis of Spectral Hypercube (FLAASH) algorithm (Thome *et al.*, 1998). The FLAASH is mathematically computed as

$$L = \left( \frac{AP}{1 - P_e S} \right) + \left( \frac{BP_e}{1 - P_e S} \right) + L_a$$

Where:

**P** is the pixel surface reflectance

**P<sub>e</sub>** is an average surface reflectance for the pixel and a surrounding region

**S** is the spherical albedo of the atmosphere

**L<sub>a</sub>** is the radiance back scattered by the atmosphere while **A** and **B** are coefficients that depend on atmospheric and geometric conditions but not on the surface.



**Fig. 2:** a) Serpentinites (SER) altered to talc-carbonate rocks intruded by alkali-feldspar granite of El Delihimmi- Nusla granites; b) Well defined foliated metasediments (MS ) poor in blocks in the NW-SE direction ; c) Foliated metasediments (MS) enclosing serpentinites (SER) and talc carbonates (TC) blocks, which are intruded by alkali-feldspar granite (AFG) d) Close up view showing exfoliation in older granitoids; e) Close up view showing quartz veinlet in monzogranite; F) Close up view showing hematitization (H) and Argillic type in syenogranite

Relative Band Depth (*RBD*) is an algorithm in which three-point ratio formulation for delineate the target feature. For each absorption feature, the numerator is the sum of the bands representing the shoulders (*S1* and *S2*) and the denominator is the band located nearest the absorption feature minimum (*T*).

$$RBD = (S1 + S2)/T \quad (\text{Gupta, 2003})$$

Band ratios (BR) is a data transformation method in which the digital number value of one band is divided by the digital number value of another band with enhances the spectral differences between bands and reduces the effects of topography (Rowan *et al.*, 1977; Goetz *et al.*, 1983 and ENVI, 2005). Spectral band ratios enhance compositional information while suppressing other types of information about earth's surface, such as terrain slope and grain size differences (Vincent, 1997).

Support Vector Machine (SVM) is a supervised classification method derived from statistical learning theory that often yields good classification results from complex and noisy data (ENVI, 2005).

Target detection wizard analysis technique of ENVI 5.3 was applied to delineate the hydrothermal alteration minerals at the study area. The analysis approach starting with data transformation using minimum noise fraction (MNF), then selecting the targets using USGS library mineral spectra and finally the production of maps using spectral mapping method. Hence, matched filtering (MF) and mixture tuned matched filtering (MTMF) were carried out on ASTER data. The methodology used in this study is summarized in figure (3). The data is processed using ENVI software (Version 5.3).

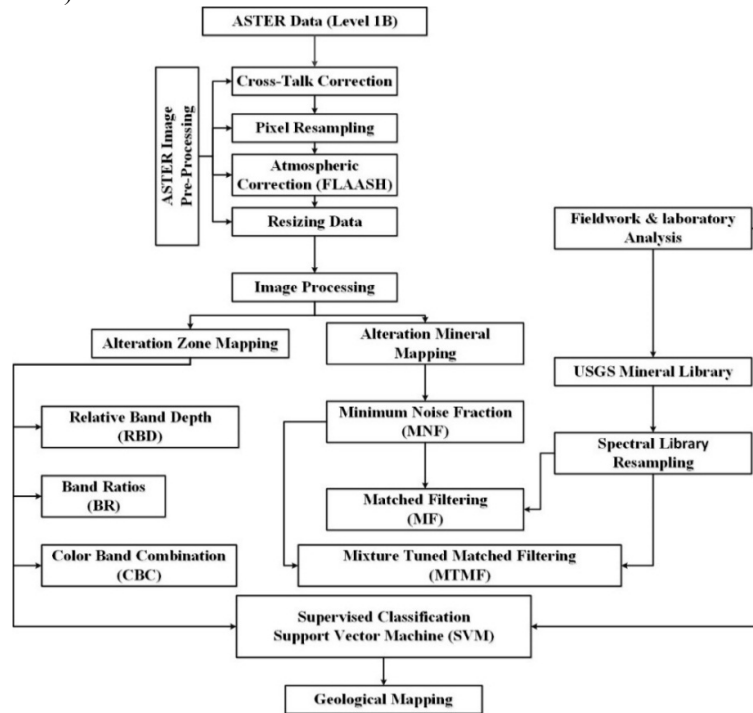


**Fig. 3:** Flowchart of the main processing steps that performed in the present study.

#### 4. Field and laboratory methods

Field survey was carried out to derive the unique view of the granitic masses through collecting samples from the granitic masses and observe relationship between them and different lithological units in the study area. More than fifty-five ground truth areas were checked and verified in the field. Nineteen thin sections, representing the younger granites as well as the older granitoids, were selected for determining the volume percentage of the rock forming minerals in the studied granites. The modal composition of the selected thin sections is listed in table (2) and the obtained data are plotted in QAP ternary diagram (Fig. 4), from which the older granitoids plot in the granodiorite field, whereas the younger granites range in composition from monzogranite through syenogranite to alkali-feldspar granite. The petrographic investigation for collected samples as well as X-ray diffraction (XRD) analysis of some altered samples was carried out revealing the presence of common alteration minerals (hematite, kaolinite, muscovite, kaolinite and chlorite) as shown in figures (5, 6 and 7). Radioactive survey was carried out in order to delineate the radiometric anomalous zones and their relation with the alteration zones. The radiometric data measured in the laboratory for 27 granitic samples of G. Abu El-Tiyur area are shown in table (3). The radiometric analysis revealed that the alkali-feldspar granite (The northern part of El-Delihimmi-Nusla granites), which significantly have higher hematite and muscovite content rather than the other exposures, are characterized by high levels of radioactivity compared with the other granitic rocks of the studied area. The uranium content within the alkali-feldspar granite ranges from 16 to 28 ppm with an average 22 ppm while the thorium content ranges from 12 to 31 ppm with an average 23.6 ppm. Thorium is three times as abundant as uranium in rocks (Rogers and Adams, 1969). When this ratio is disturbed, it indicates a depletion or enrichment of uranium. The granodiorite, monzogranite and alkaline (riebeckite) granite

show eTh/eU average ratios higher than three (5.1, 3.5 and 4.2 respectively) suggesting uranium depletion. On the other hand, syenogranite and alkali-feldspar granite show eTh/eU average ratios lower than three (2.5 and 1.1 respectively) suggesting uranium addition. The minimum, maximum and averages of eU, eTh, Ra and eTh/eU in the granitic rocks are shown in figure (8).

**Table 2:** Modal analysis of the studied granitic rocks of G. Abu El-Tiyur area, CED, Egypt

Rock units	Rock type	S. No.	Mineral Constituents					
			Alkali-feldspars	Plag.	Quartz	Mafic	Alkali amphiboles	Acces.
Older Granitoids	Grano diorite	1	16	45.6	30.2	6.1	-	2.1
		2	15.3	49.4	27.5	5.9	-	1.9
		3	17.3	46.5	27.4	7.5	-	1.3
Younger Granites	Monzo granite	4	26.4	27.5	39.4	4.8	-	1.9
		5	28.1	29	36.3	4.4	-	2.2
		6	21	34.6	38.9	4	-	1.5
	Syeno granite	7	20.2	36.1	37.4	4.7	-	1.6
		8	53.1	10.3	32.6	3	-	1
		9	51.8	11.2	33.4	2	-	1.6
	Alkali-feldspar granite	10	60	5.1	30	2.7	-	2.2
		11	63.7	3.1	30.5	1.7	-	1
		11	62.3	3.5	31.2	2.2	-	0.8
		12	65.4	4.2	26.3	0.9	1.2	2
		13	60	5.1	30	1.0	1.4	2.5
		14	67.4	4.8	24.5	0.6	1	1.7
		15	65	4.9	26.3	0.5	1.3	2
		16	66	4.4	26	1	1.1	1.5
		17	66.3	2.5	28	0.7	0.86	1.64
		18	66.5	2.9	27.5	0.8	1	1.3
19	68.1	4.6	24.7	0.6	0.9	1.1		

S. No = Sample number; Plag. = Plagioclase; Mafic (micas, chlorite and hornblende); Acces. = Accessories (zircon, apatite, opaques, fluorite and sphene, ...); Alkali amphiboles = Riebeckite + Arfvedsonite

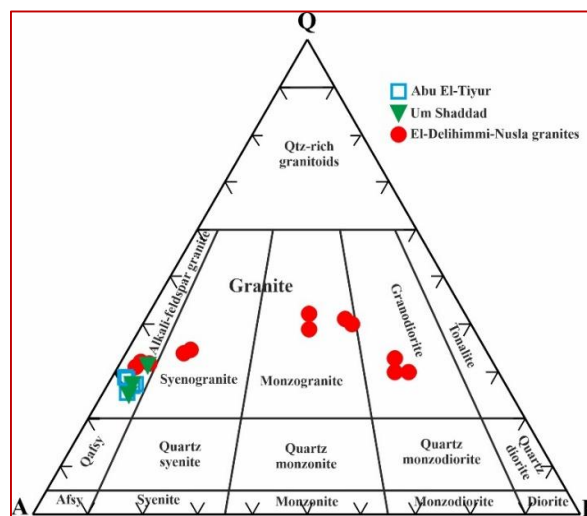


**Fig. 4:** Modal composition (QAP-diagram) for the granitic rocks of G. Abu El-Tiyur area, CED, Egypt (after Streckeisen, 1976).

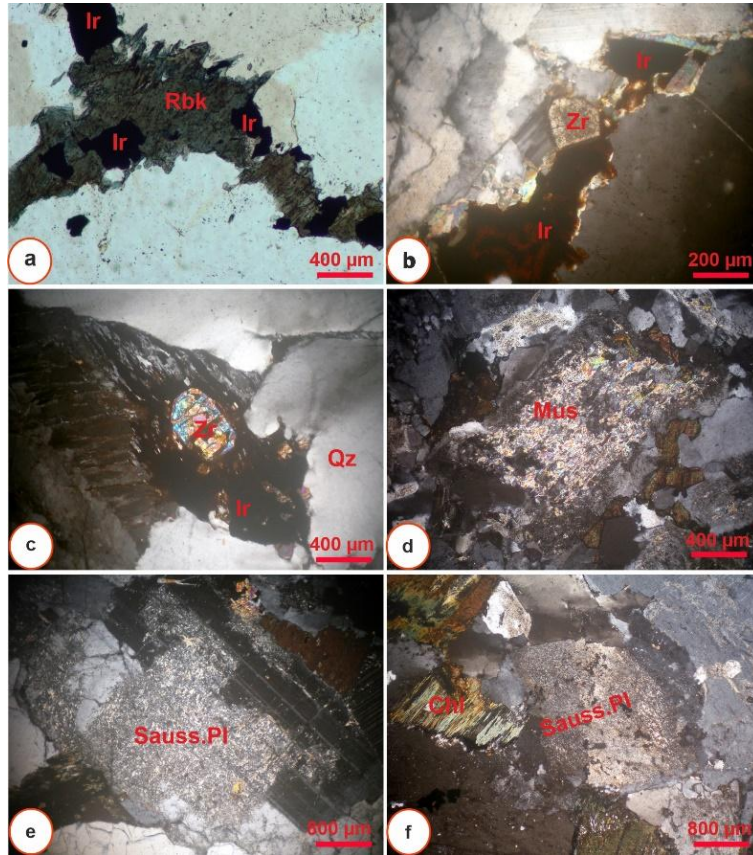


**Fig. 5:** a) Alkali-feldspar granite is showing anhedral riebeckite crystals (Rbk) enclosing iron oxyhydroxides (Ir), C.N.; b) Euhedral zircon crystal (Zr) associated with opaques and quartz in alkali-feldspar granite, C.N.; c) Metamictic zircon (Zr) with opaques (Ir) interstitially between perthite and quartz (Qz), syenogranite, C.N.; d) Zoned plagioclase crystal with selective alteration (muscovitization), alkali-feldspar granite C.N.; e) Partially saussuritized plagioclase crystal (Sauss.Pl), monzogranite C.N.; f) Completely saussuritized plagioclase (Sauss.Pl) associated with chloritized biotite (Chl), granodiorite, C.N.

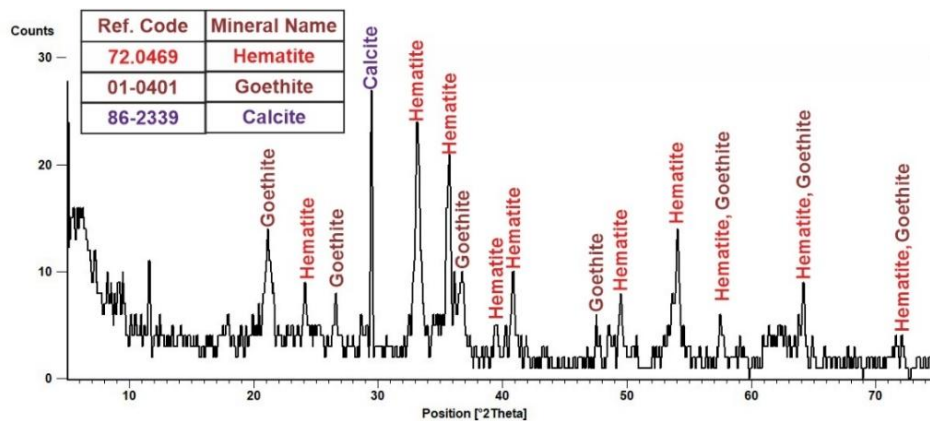


**Fig. 6:** XRD pattern of hematite and goethite, G. Abu El-Tiyur area, CED, Egypt.

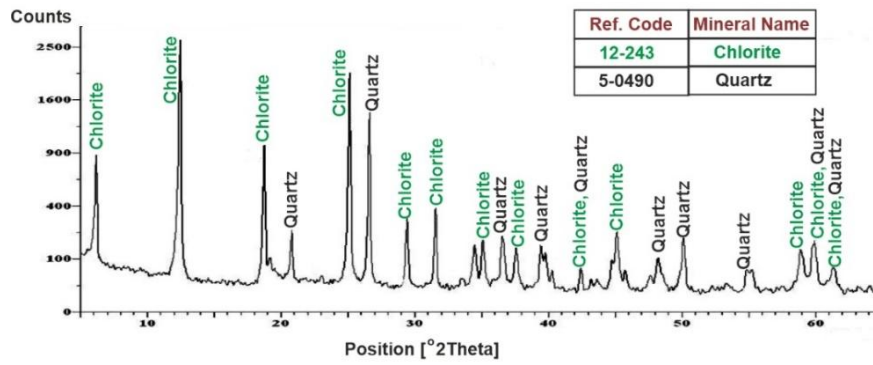
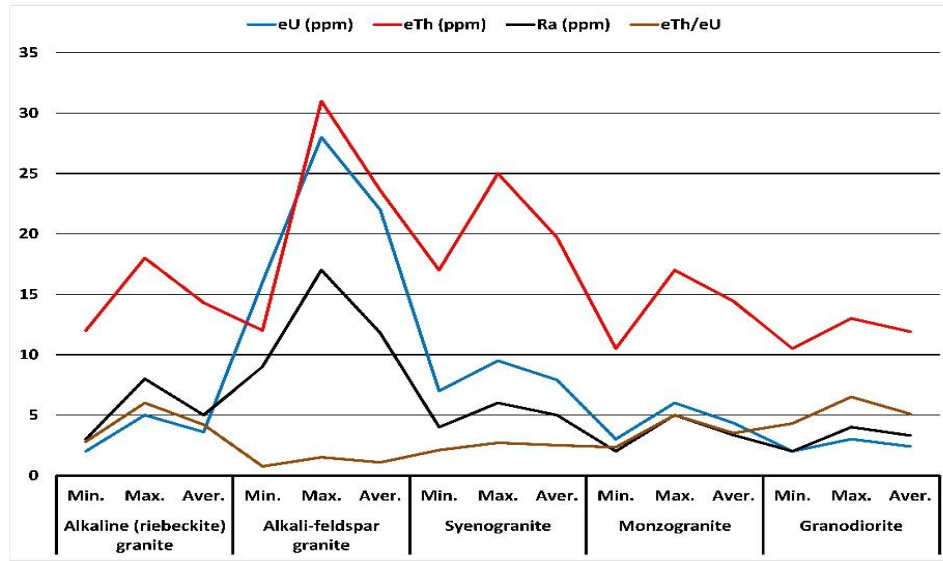


Fig. 7: XRD pattern of chlorite and quartz, G. Abu El-Tiyur area, CED, Egypt.

**Table 3:** eU, eTh, Ra and eTh/eU of the of the granitic samples of G. Abu El-Tiyur area, CED, Egypt

Rock units	Rock type	S. No.	eU (ppm)	eTh (ppm)	Ra (ppm)	eTh/eU
Late to post-collision granites	Alkaline (riebeckite) granite	1	4.5	13	3	3.0
		2	5	14	5	2.8
		3	2	12	4	6.0
		4	3	17	8	5.7
		5	4	18	4.5	4.5
		6	3.5	12.5	6	3.6
		7	4	14	4	3.5
		8	3	14	5.5	4.7
	Alkali-feldspar granite	9	27	26	11	1.0
		10	18	27	9	1.5
		11	28	31	17	1.1
		12	16	12	13	0.8
		13	21	22	9	1.0
	Syenogranite	14	9.5	25	5	2.6
		15	7	19	5	2.7
		16	8	17	6	2.1
		17	7	17	4	2.4
	Monzogranite	18	4	10.5	4	2.6
		19	3.5	14	2	4.0
		20	4	16	3	4.0
		21	6	14	5	2.3
		22	3	15	3	5.0
		23	5.5	17	3	3.1
Arc granitoids	Granodiorite	24	2	13	4	6.5
		25	3	13	4	4.3
		26	2	10.5	2	5.3
		27	2.5	11	3	4.4



**Fig. 8:** Line diagram showing minimum, maximum and averages of eU, eTh, Ra and eTh/eU in the granitic rocks of G. Abu El-Tiyur area, CED, Egypt.

### 5. Identification of hydrothermal alteration types

Identification the types of hydrothermal alterations and their alteration zones are achieved through the utilization of some different image processing including; color band composites as well as data transformation techniques such as; a) relative band depth, b) band ratios, and c) minimum noise fraction.

#### 5.1. Relative Band Depth (RBD)

The Al-OH group minerals has an intense diagnostic spectral absorption feature centered at (2.20  $\mu\text{m}$ ) coinciding with ASTER band 6 (2.185–2.225  $\mu\text{m}$ ) and reflectance peaks in neighboring band 5 (2.145-2.185  $\mu\text{m}$ ) and band 7 (2.235-2.285  $\mu\text{m}$ ). Hence, RBD [(b5 + b7)/ b6] used for targeting the mineral assemblages of phyllic alteration zones. Mg-OH group minerals and/ or carbonate minerals show intense diagnostic spectral absorption feature centered at (2.35  $\mu\text{m}$ ), which coincide with ASTER band 8 (2.295-2.365  $\mu\text{m}$ ) and reflectance peaks in band 7 (2.235-2.285  $\mu\text{m}$ ) and band 9 (2.360-2.430  $\mu\text{m}$ ) so that ASTER RBD [(b7+b9)/ b8] was created for mapping the mineral assemblages of propylitic alteration zones. Fe-O and Fe-OH minerals show charge transfer and Fe<sup>3+</sup> crystal field bands between VNIR wavelength ranges. Similarly, RBD [(b2+b3)/b1] was created to enhance areas rich in iron oxides and hydroxides minerals.

Color composite image of the three RBDs [(b2+b3)/b1, (b7+b9)/b8 and (b5+b7)/b6] in RGB representing Iron oxides/ hydroxides, propylitic and phyllic alteration respectively, was created to enhance and facilitate the visual interpretation (Fig.9). In this way, alteration mineral assemblage can be identified through different colors. Phyllic alteration zones manifested as light purple color, propylitic alteration zones as green and finally the areas that rich in iron oxides and hydroxides manifested as brownish red. ASTER SWIR false color image that created by combined bands 4, 6 and 8 in RGB respectively (Fig.10), displays phyllic alteration in a brownish red and pale magenta color and propylitic alteration in yellowish green and dark aqua marine color. These images revealed that the propylitic alteration is dominant in the ophiolitic assemblage while both phyllic alteration and iron oxides/ hydroxides are dominant in the granitic rocks with a great noticeable abundant at the alkali feldspar granite.

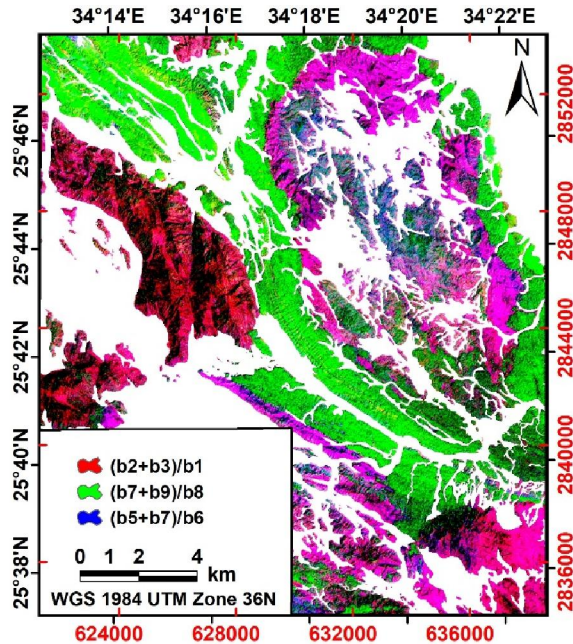


**Fig. 9:** False color composite ASTER image of iron oxides, propylitic and phyllic in RGB of G. Abu El-Tiyur area, CED, Egypt

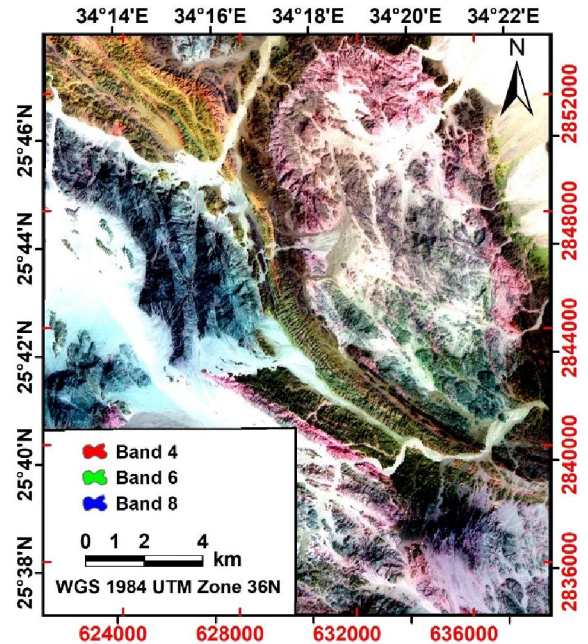


**Fig. 10:** False color composite ASTER image bands 4,6,8 in RGB of G. Abu El-Tiyur area, CED, Egypt

### 5.2. Band Ratios (BRs)

Muscovite and sericite  $[K Al_3 Si_3 O_{10} (OH)_2]$  are the main indicator minerals for mineral assemblages of phyllic alteration zones, which yields an intense (Al-OH) absorption feature centered at ASTER band 6 (Fig. 11). Sericite is a term that is used to describe fine-grained white mica (muscovite or paragonite). Such micas are not necessarily chemically different from muscovite although they often have high  $SiO_2$ ,  $MgO$  and  $H_2O$  and low  $K_2O$ . Band ratio  $b7/b_6$  was used for (Al-OH) enhancement (Fig. 12). Chlorite  $[(Mg, Al, Fe)_{12}[(Si, Al)_8O_{20}](OH)_{16}]$  is an indicator mineral for mineral assemblages in the propylitic alteration.

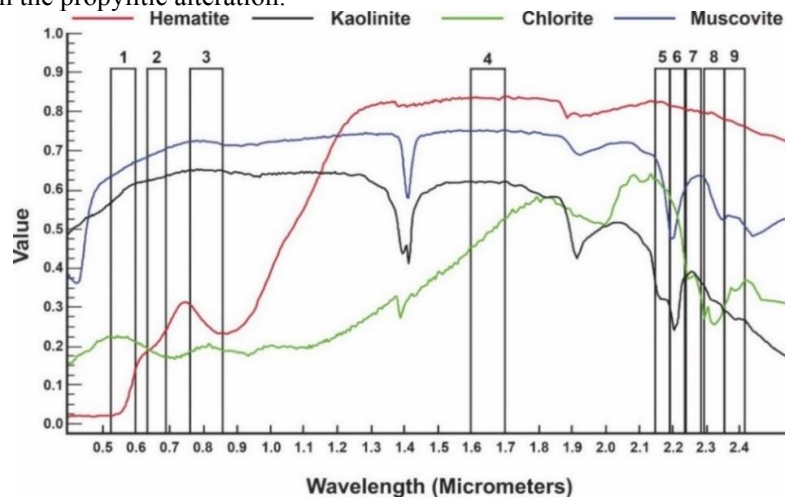


**Fig. 11:** The USGS library of the studied minerals superimposed on ASTER band intervals in the VNIR-SWIR region

Propylitic alteration exhibits absorption feature centered ASTER band 8 caused by (Mg-OH). Band ratio  $b9/b_8$  was used for (Mg-OH) enhancement (Fig. 13). Kaolinite group minerals

[Al<sub>2</sub>Si<sub>2</sub>O<sub>5</sub>(OH)<sub>2</sub>] are the main indicator minerals for mineral assemblages of argillic alteration zones, which yields an intense (Al-OH) absorption feature centered at ASTER band 6 and ASTER band 5 (2.145-2.185 μm). Band ratio b5/ b6 was used for (Al-OH) enhancement (Fig.14). Finally, areas rich in iron oxides and hydroxides delineated using band ratio b2/b1 (Fig.15). The relative band depth and band ratios used in this study is summarized in Table (4).

**Table 4:** Relative band depth (RBD) and Band ratios (BRs) used to discriminate alteration minerals within G. Abu El-Tiyur area, CED, Egypt.

Mineral composition	Pathfinder minerals	Formula	References
<b>Relative Band Depth (RBD)</b>			
Al-OH	Muscovite, illite and smectite	(b5 + b7)/ b6	Rowan <i>et al.</i> , 2003
Mg-OH	Chlorite, epidote and carbonates	(b7+b9)/ b8	Rowan <i>et al.</i> , 2003
Fe-O and Fe-OH minerals	Hematite, goethite	(b2+b3)/b1	Badr, 2017
<b>Band ratios (BRs)</b>			
	Muscovite and sericite	b7/ b 6	Hewson <i>et al.</i> , 2005
Al-OH	Kaolinite group	b5/ b 6	Hewson <i>et al.</i> , 2005
Mg-OH	Chlorite	b9/b8	Mars and Rowan, 2010
Fe-O and Fe-OH minerals	Hematite; goethite	b2/b1	Rowan <i>et al.</i> , 2005

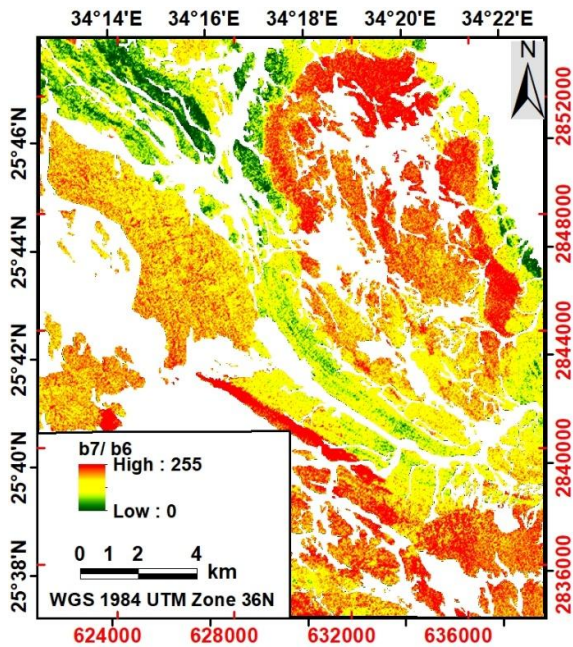


**Fig. 12.** ASTER band ratio b7/b6 image showing mineral assemblages of phyllic alteration zones within G. Abu El-Tiyur area, CED, Egypt

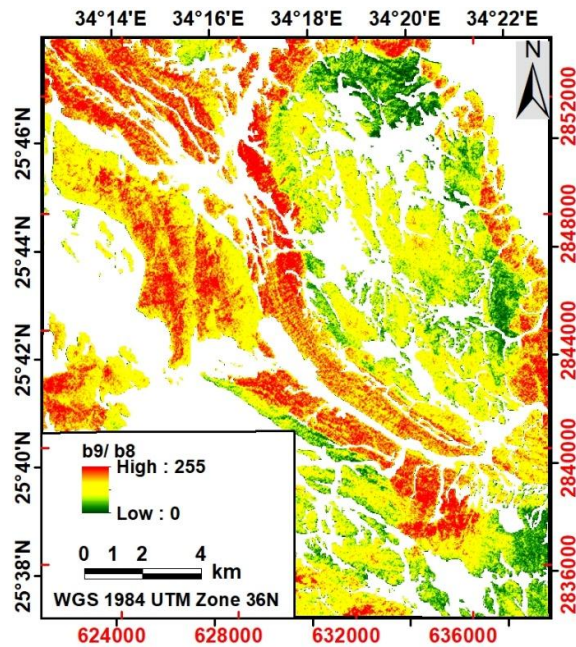


**Fig. 13.** ASTER band ratio b9/b8 image showing mineral assemblages of propylitic alteration zones within G. Abu El-Tiyur area, CED, Egypt

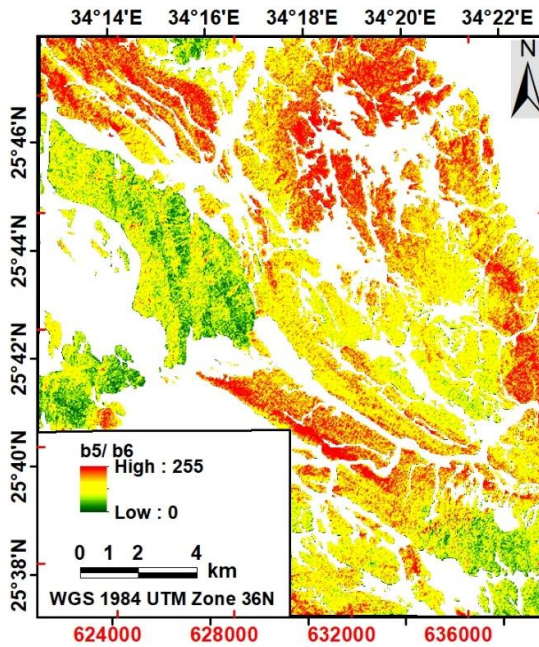


**Fig. 14.** ASTER band ratio b5/b6 image showing mineral assemblages of argillic alteration zones within G. Abu El-Tiyur area, CED, Egypt

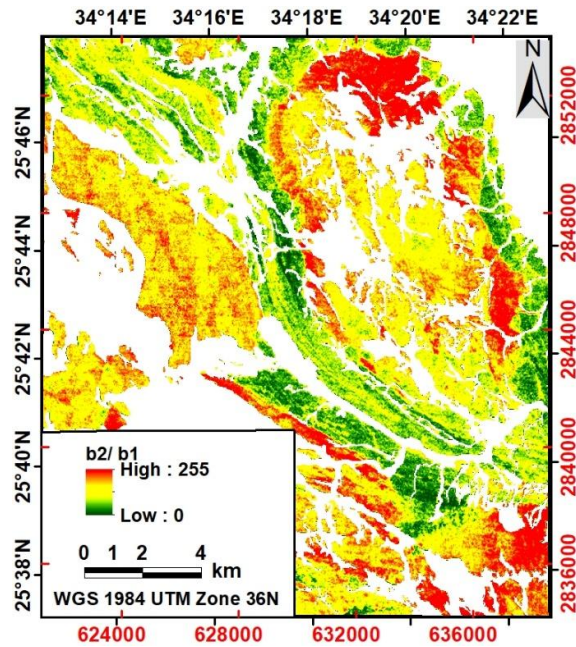


**Fig. 15.** ASTER band ratio b2/b1 image showing iron oxides and hydroxides within G. Abu El-Tiyur area, CED, Egypt

### 5.3. Minimum Noise Fraction (MNF)

MNF data transformation technique was applied to the nine (VNIR-SWIR) bands in order to decrease the dimensionality and segregated the noise that leads to effectively extract the end members and mapping hydrothermal alteration minerals as well as discriminate lithological units. The resulting bands of the MNF transformed data ranked with the largest amount of variance in the first bands and decreasing data variance with increasing band number. According to Boardman and Green (2000), the eigenvalue of each MNF transformed band is a reflection of its information content. Jensen (2005) stated that the MNF eigen images with values close to one contain mostly noise and usually excluded from the data. Figure (16) shows the eigenvalues of the nine output MNF eigen images.

The statistic results derived from VNIR-SWIR band revealed that the MNF eigen images of bands 7, 8 and 9 are not suitable for assigning RGB color composite because of their percentage of eigenvalues close to one. A color composite image of MNF bands 1, 2 and 3 in RGB is shown in figure (17). The image discriminates hydrothermal alteration zones rich in iron oxides and hydroxide minerals (turquoise color) and areas rich in phyllic alteration assemblage (purple color) whereas those rich in propylitic alteration assemblage (red color). The location of detected alteration zones by MNF data transformation technique is coincided with that enhanced by combined bands 4, 6 and 8 in RGB. The image also discriminates the different rock units with accurate tracing their contacts especially the granitic rocks. Late to post-collision granites are differentiated into four varieties; a) monzogranite, b) syenogranite, c) alkali-feldspar granite and d) alkaline (riebeckite) granite.

### 5.4. Spectral Mapping

The relative abundance of the target minerals in this study were delineated by Two spectral mapping algorithm matched-filtering (MF) and matched tuned matched filter (MTMF) using the end member minerals from United States Geological Survey (USGS) library mineral spectra (Fig.18).

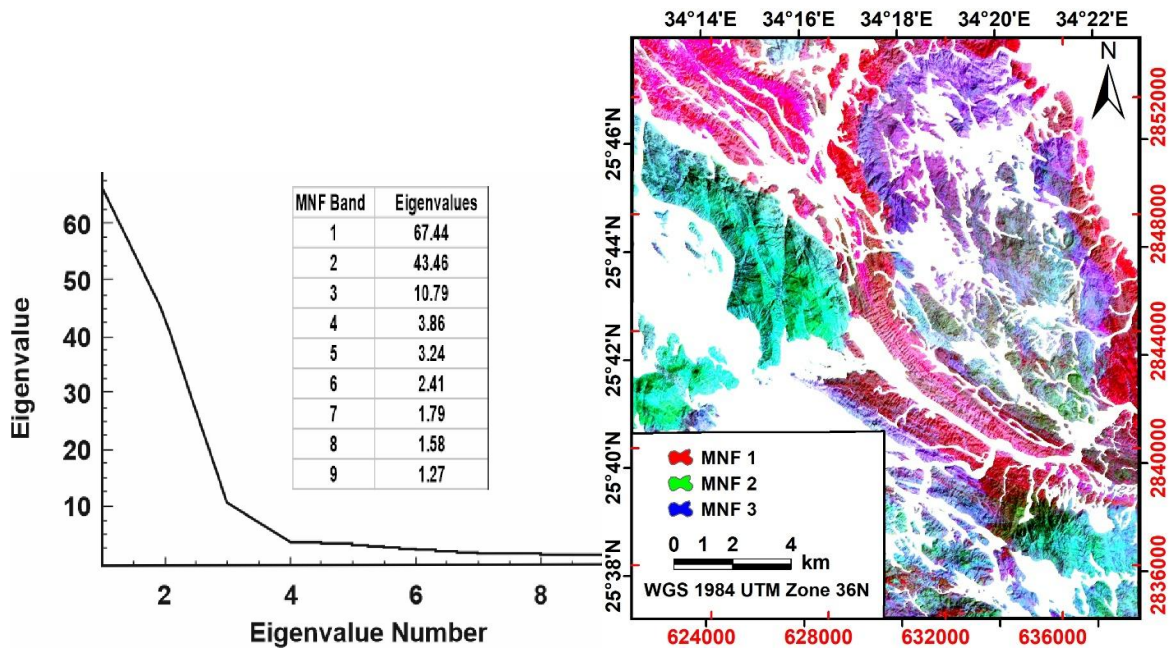


**Fig. 16.** The MNF eigenvalues plot of the 9 Eigen images of ASTER VNIR-SWIR data of G. Abu El-Tiyur area, CED, Egypt

**Fig. 17.** Color composite image of MNF Eigen images 1, 2 and 3 in RGB of G. Abu El-Tiyur area, CED, Egypt

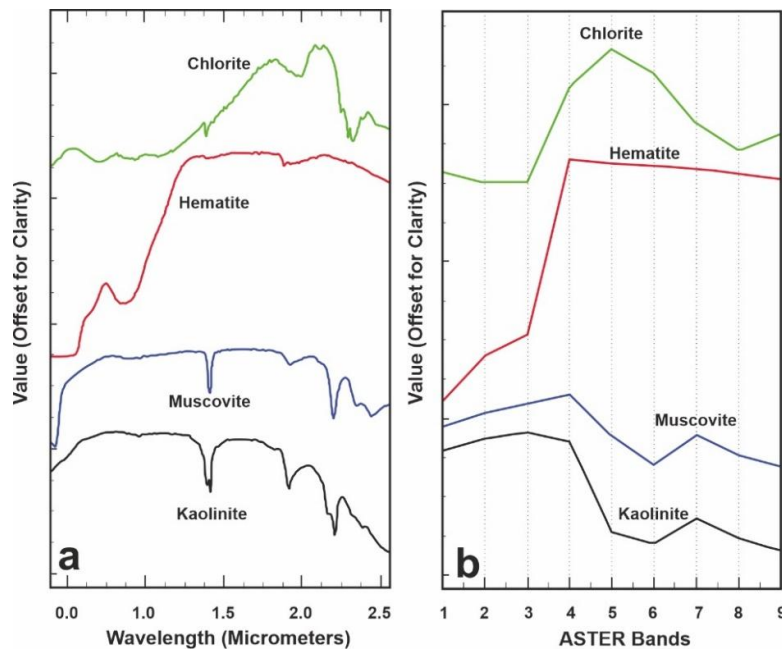


**Fig. 18.** a) Laboratory spectra of chlorite, hematite, muscovite and kaolinite minerals from the USGS spectral library b) Spectral curve of the four minerals resampled to ASTER band passes

#### 5.4.1. Matched-Filtering (MF)

MF is a technique that creates a partial unmixing of spectra to estimate the abundance of user-defined end-members from a set of reference spectra. This technique maximizes the response of the known end-member and suppresses the response of the composite unknown background, thus matching the known signature (Harsanyi *et al.*, 1994 and Boardman *et al.*, 1995). MF algorithm revealed four MF scores in grey scale images (Figs. 19, 20, 21 and 22) indicating the degree of how well unknown pixel was matched with selected end-member minerals. The brighter pixel means a

perfect match and such areas mostly contain alteration minerals (Research System Inc., 2008). These images revealed that the hematite and muscovite are mainly concentrated within the granitic rocks with a great noticeable abundance in alkali-feldspar granite. Chlorite and kaolinite show a wide distribution in the studied area with a noticeable abundance of chlorite in metasediments poor in blocks while the kaolinite show increase content in serpentinites and metasediments rich in blocks.

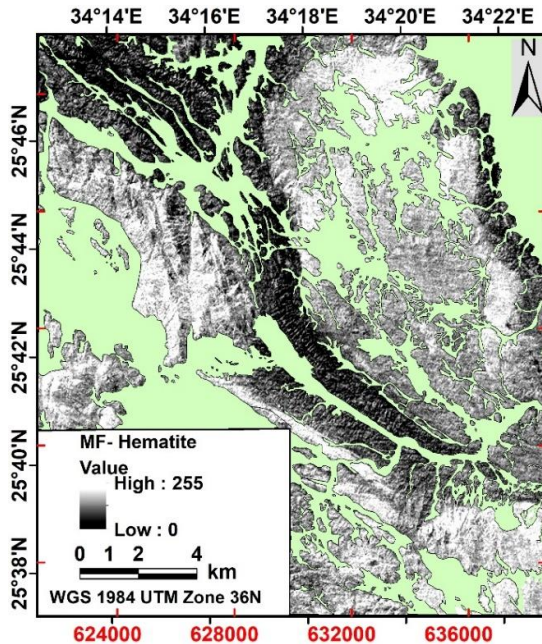


Fig. 19. MF score image showing the distribution of hematite end-member mineral within G. Abu El-Tiyur area, CED, Egypt

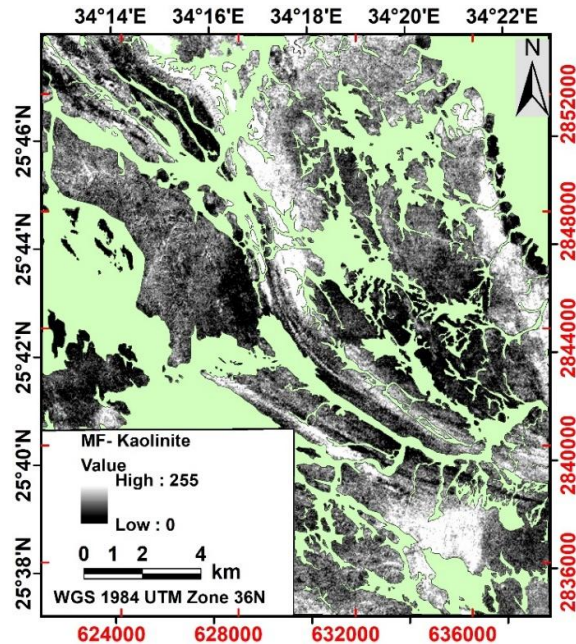


Fig. 20. MF score image showing the distribution of kaolinite end-member mineral within G. Abu El-Tiyur area, CED, Egypt

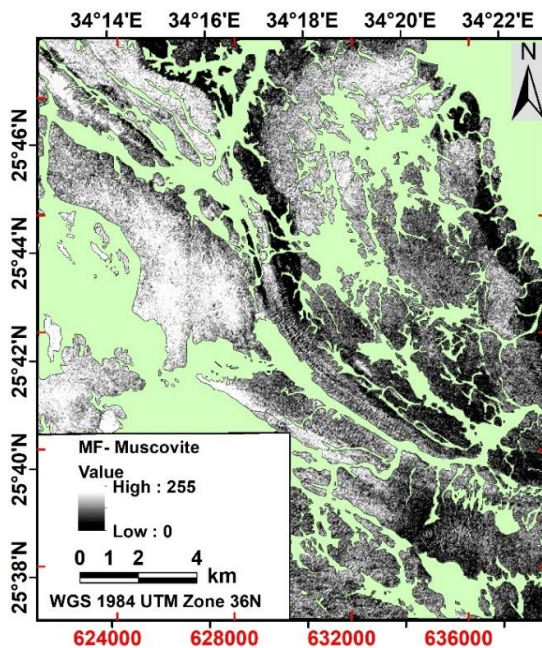


Fig. 21. MF score image showing the distribution of muscovite end-member mineral within G. Abu El-Tiyur area, CED, Egypt.

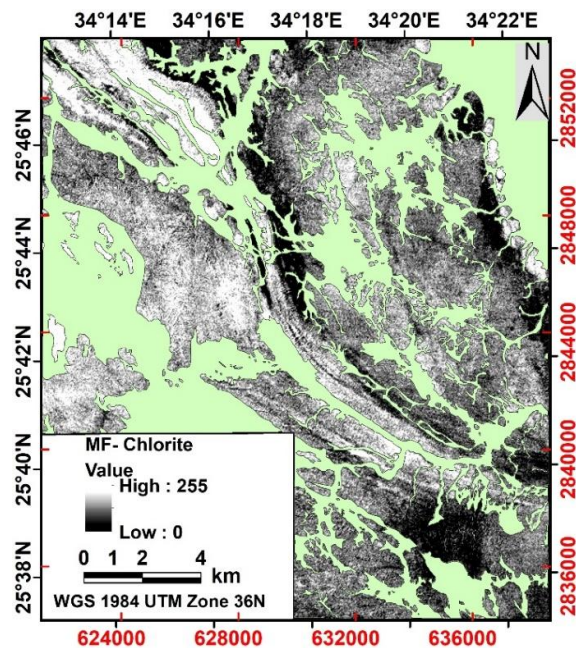


Fig. 22. MF score image showing the distribution of chlorite end-member mineral within G. Abu El-Tiyur area, CED, Egypt.

#### 5.4.2. Mixture-Tuned Matched-Filtering (MTMF)

MTMF technique is a combination of the Linear Spectral Unmixing technique and the statistical Matched Filtering model (Boardman, 1998). The advantage of MTMF is its ability to map a single known target without knowing the other background end-member signatures. The result of MTMF method presented by pixels abundance with different color for each end member minerals (Figs .23 and 24). The results of MTMF algorithm are similar to the obtained ones by MF algorithm. The resulted MTMF grey scale images were subjected to post classification using rule classifier method and the low concentrates are excluded by calculating the threshold. The anomalous concentrates (at confidence level 99%) of hematite, muscovite, chlorite and kaolinite are presented as red, blue, green and purple pixel colors respectively. Images revealed that the highest concentration of hematite is found within the northern parts of El-Delihimmi granites (alkali-feldspar granite). Kaolinite shows its great abundance in serpentinite rocks. The highest concentration of chlorite in the study area is present within the metasediments poor in blocks and serpentinites while muscovite is mainly concentrated in the alkali-feldspar granite.

#### 6. Supervised classification

The remote sensing images have been verified in the field through more than 65 ground truth area (training samples) represent all rock unites cropping out in the study area with focusing on granitic rocks. After masking Quaternary sediments (wadis), supervised areas of interests (AOIs) are selected and controlled to the exposed basement rock units. The supervised classification processed using the Support Vector Machine (SVM) method. The output is shown in figure (25). Ten classes are given with ten colors each is corresponding to a certain rock unit. Metaultramafites (black), metasediments poor in blocks (green), metasediments rich in blocks (magenta), metagabbros (blue), older granitoids (yellow), monzogranite (brown), syenogranite (pink), alkali-feldspar granite (red), alkaline (riebeckite) granite (orange) and wadi deposits (white).

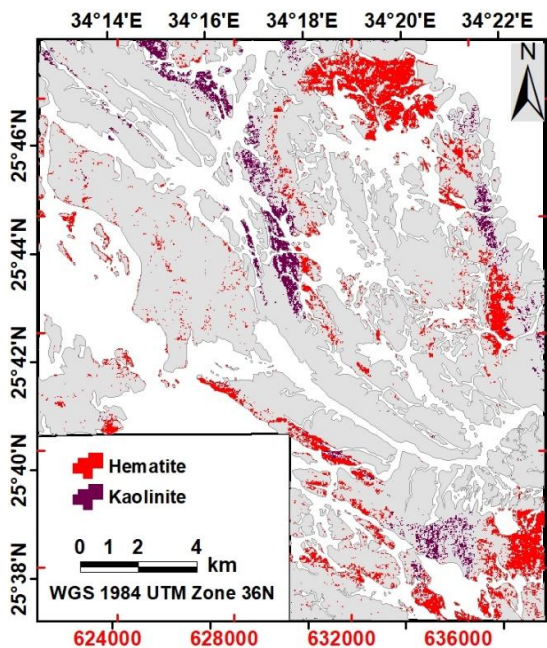


Fig. 23. Results of MTMF sub-pixel abundance for hematite and kaolinite end members used as reference, G. Abu El-Tiyur area, CED, Egypt

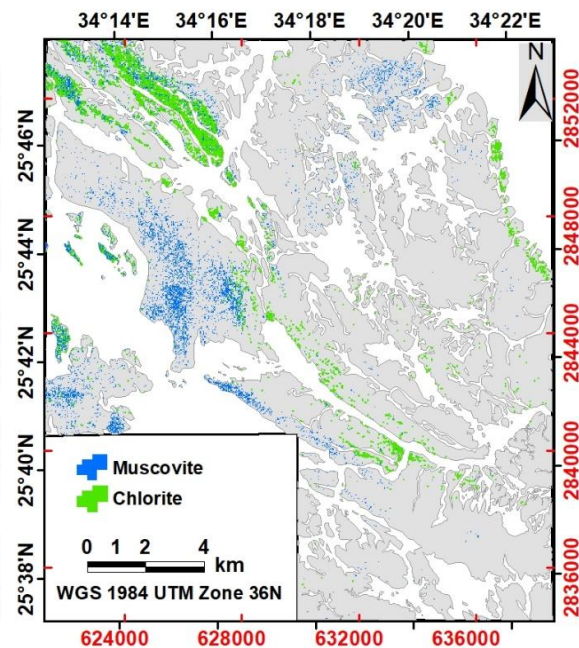


Fig. 24. Results of MTMF sub-pixel abundance for muscovite and chlorite end members used as reference, G. Abu El-Tiyur area, CED, Egypt

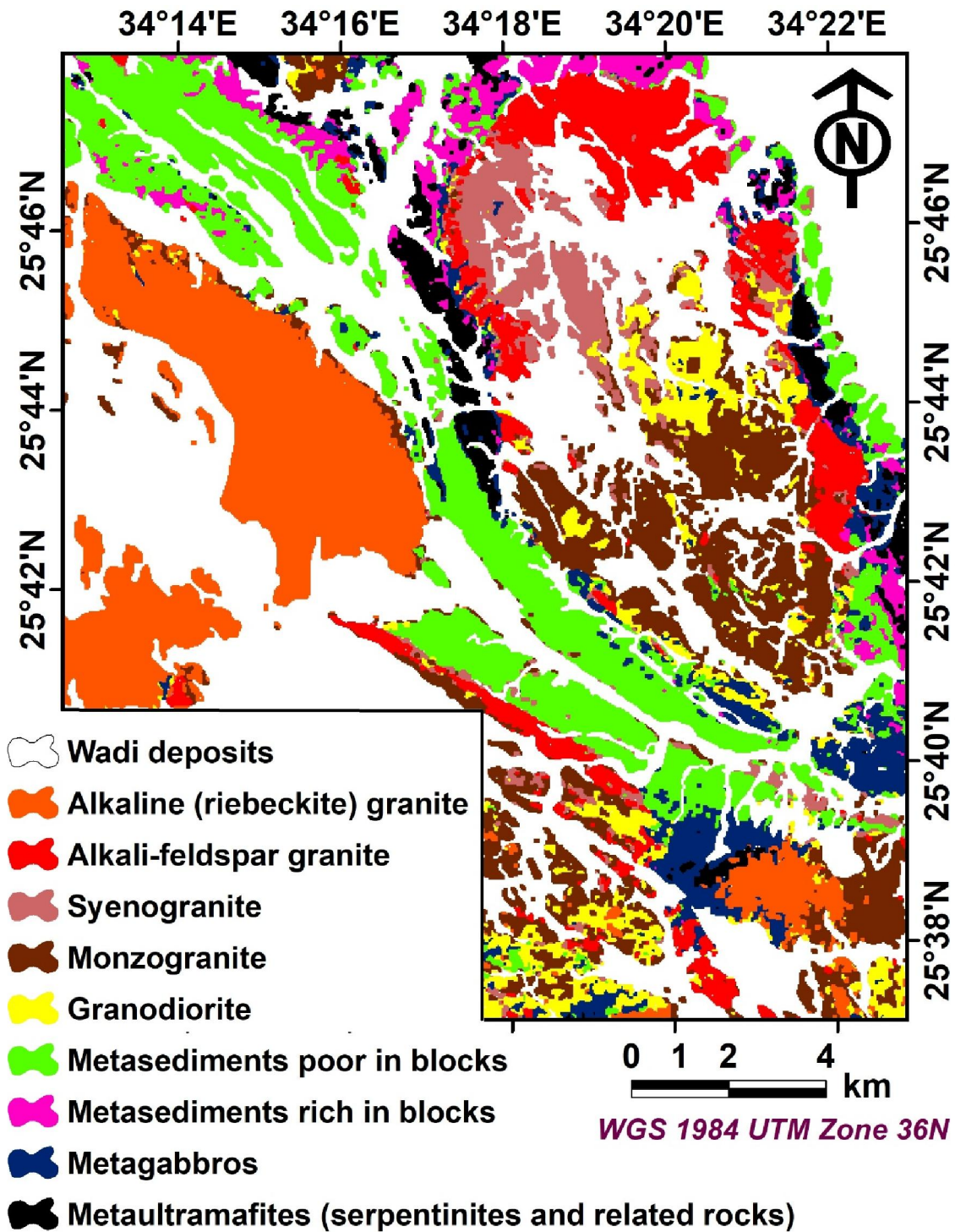


Fig. 25: Supervised classification image of G. Abu El-Tiyur area, CED, Egypt

## 7. Conclusions

G. Abu El-Tiyur area, as a part of the CED of Egypt comprises a variety of basement rocks including three petro-tectonic assemblages; 1) The allochthonous ophiolitic assemblage, which is including dismembered ophiolitic rocks represented by metaultramafites - serpentinites and related rocks - and metagabbros blocks and fragments embedded in metasediments, which are differentiated in the present study into; a) Metasediments rich in blocks and b) metasediments poor in blocks; 2) Arc Granitoids are mainly represented by granodiorite, which were controversially mapped previously sometimes as older granitoids or as younger granites; 3) Late to post-collision granites are represented by G. Abu El-Tiyur, G. Um Shaddad, and El Delihimmi- Nusla granites (monzogranite, syenogranite, alkali-feldspar granite and alkaline (riebeckite) granite).

G. Abu El-Tiyur is previously mapped either as a) cataclastic granites; b) biotite granite, riebeckite granite and alkali-feldspar granite; c) alkali-feldspar granite and d) alkaline granite whereas the present study revealed that it is mainly represented by alkaline (riebeckite) granite. G. Um Shaddad is previously mapped either as a) monzogranite and/or syenogranite; b) perthitic leucogranite and c) alkali-feldspar granite whereas the present study revealed that it is mainly represented by alkaline (riebeckite) granite (the central part), monzogranite (the eastern part) with minor alkali-feldspar granite (the southwestern part). El Delihimmi- Nusla granites are previously mapped either as a) granodiorite and muscovite granite; b) late- to post-orogenic granite and originated due to magmatic differentiation; c) biotite granite and muscovite granite; d) granodiorite; e) monzogranite; f) alkali-feldspar granite gneissic in parts. The present study differentiated El Delihimmi- Nusla granites into granodiorite, monzogranite and syenogranite at the core of the intrusion while the outer peripheries are mainly alkali-feldspar granite except the south parts of this granitic intrusion.

ASTER relative band depths  $[(b5+b7)/b6, (b7+b9)/b8 \text{ and } (b2+b3)/b1]$  have been effectively used in delineating the alteration mineral assemblage phyllic and propylitic in addition to areas rich in iron oxides and hydroxides respectively. ASTER band ratios  $[b7/ b 6, b9/ b 8, b5/ b 6 \text{ and } b2/b1]$  were efficient in detecting muscovite, chlorite, kaolinite group minerals and areas rich in iron oxides and hydroxides respectively.

The relative abundance of the target minerals in this study were delineated by two spectral mapping algorithms (matched-filtering and matched tuned matched filter). Hematite is mainly concentrated within the alkali feldspar granite represented by the outer parts of El-Delihimmi-Nusla granites, while muscovite is mainly concentrated in the alkaline (riebeckite) granite and the alkali-feldspar granite. Kaolinite and chlorite show a wide distribution in the area with a great noticeable concentration in the ophiolitic assemblage.

The field observations as well as the petrographic investigations are in complete harmony with the interpretation of the obtained images resulted from remote sensing processing of ASTER VNIR-SWIR data. The alkali-feldspar granite exhibits the highest radioactivity in the area with maximum radioactive contents 18 ppm and 31 ppm for eU and eTh respectively, which significantly have higher hematite and muscovite content rather than the other granitic exposures.

The integration between field observation, petrographic investigations and the processed ASTER images resulted in discrimination the granitic rocks in G. Abu El-Tiyur area into granodiorite, monzogranite, syenogranite, alkali-feldspar granite and alkaline (riebeckite) granite. A new detailed geological map of G. Abu El-Tiyur area (scale 1:100,000) is constructed depending on the integration between the processed ASTER images, field observation and petrographic investigations (Fig.26).

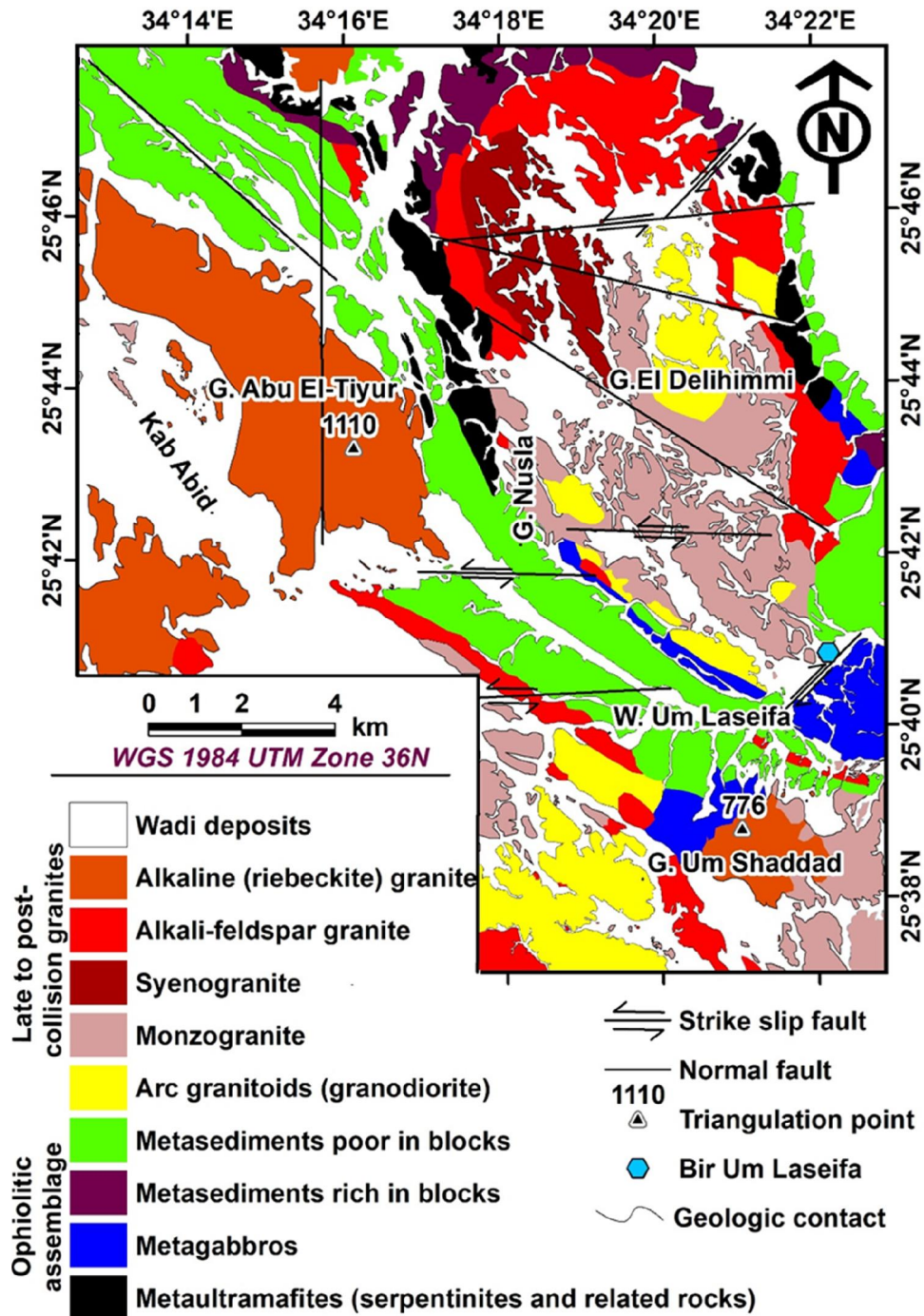


**Fig. 26:** A detailed new geological map of G. Abu El-Tiyur area, CED, Egypt; produced from the integration of ASTER VNIR-SWIR data, field observations and petrographic studies.

## References

Abd El-Wahed, A.A., S.E. Ammar, T.F. Youssief, and M.O. El-Husseiny, 2002. Petrography, REE geochemistry and Rb-Sr isotopes study of Abu Tiyur granite, Central Eastern Desert, Egypt. M.E.R.C., Ain Shams Univ., Earth Sci. Ser. 16: 16-24.

- Abdel Meguid, A.A., 1992. Late Proterozoic Pan African tectonic evolution of the Egyptian part of the Arabian Nubian Shield. M. E. R. C. Ain Shams Univ., Earth Sc. Ser. 6: 13-28.
- Abrams, M.J., D. Brown, L. Lepley, and R. Sadowski, 1983. Remote sensing of porphyry copper deposits in Southern Arizona. *Econ. Geol.* 78: 591–604.
- Akaad, M.K., and A.M. Abu El Ela, 2002. Geology of the basement rocks in the eastern half of the belt between latitudes 25 300 and 26 300N Central Eastern Desert, Egypt. The Egyptian Geological Survey and Mining Authority, Cairo, Paper No. 78.
- Badr, Y.S., 2017. Application of remote sensing technique in geologic mapping of hydrothermal alteration zones and possible radioactive potentialities at Ras Barud - Um Tagher area, North Eastern Desert, Egypt. Ph.D. Thesis, Faculty Science, Menoufiya University, Egypt.
- Bakhit, F.S., 1978. Geology and radioactive mineralization of Gabal El-Missikat area, Eastern Desert, Egypt. Ph.D. Thesis, Fac. of Sc., Cairo Univ., Cairo, Egypt.
- Boardman, J. W., and R.O. Green, 2000. Exploring the spectral variability of the earth as measured by AVIRIS in 1999, in: *Summaries of the Ninth Annual JPL Airborne Geosciences Workshop*. Jet Propulsion Laboratory Special Publication.18, 10.
- Boardman, J.W., 1998. Leveraging the high dimensionality of AVIRIS data for improved sub-pixel target unmixing and rejection of false positives: mixture tuned matched filtering. *Summaries of the Seventh Annual JPL Airborne Geoscience Workshop*, Pasadena, CA. 55.
- Boardman, J.W., F.A. Kruse, and R.O. Green, 1995. Mapping target signatures via partial unmixing of AVIRIS data, summaries. *Proceedings of the Fifth JPL Airborne Earth Science Workshop*, 23–26 January, Pasadena, California, JPL Publication 95–1, 1:23–26.
- Clark, R.N., 1999. Spectroscopy of Rocks and Minerals, and Principles of Spectroscopy, in *Manual of Remote Sensing*, Volume 3, *Remote Sensing for the Earth Sciences*, (A.N. Rencz, ed.) New York, John Wiley and Sons. 3-58.
- El Gaby, S., 1975. Petrochemistry and geochemistry of some granites from Egypt. *Neues Jahrbuch fur Mineralogie Abhandlungen*, 124 (2): 147-189.
- El Ramly, M.F., R.O. Greiling, A.A. Rashwan, and A.H. Rasmy, 1993. Geologic map of Wadi Hafifit area. Scale 1: 100:000, Egyptian Geologic Survey.
- El-Husseiny, M.O., 2003. Geology, geochemistry and distribution of uranium and thorium in Gabal Nusla area, Central Eastern Desert, Egypt. Ph.D. Thesis, Fac. Sci., Ain Shams Univ., Egypt.
- El-Kalioubi, B.A., A.I. Ragab, and Z.N. El-Alfy, 1995. Origin and tectonic environment of the Pan-African rocks of Abu El Tiyur area, Eastern Desert, Egypt. *Qatar Univ. Sci. J.*15 (2): 407-417.
- El-Kassas, I.A., 1974. Radioactivity and geology of Wadi Atalla area. Eastern Desert of Egypt, Arab Republic of Egypt. Ph.D. Thesis, Fac. of Sci., Ain Shams Univ., Cairo, Egypt.
- EL-Sherif, A.M., 2015. Contributions to the Chemical Modeling of Some Granitic Masses in the Central Eastern Desert, Egypt. *Al Azhar Bulletin of Science*. 26(2): 97 – 110.
- ENVI, 2005. ENVI user’s guide. Research System, Inc. Colourado, U.S.A., 1150.
- Fowler, A., H. Khamees, and H. Dowidar, 2007. El Sibai gneissic complex, Central Eastern Desert, Egypt: Folded nappes and syn-kinematic gneissic granitoid sheets – not a core complex. *Journal of African Earth Sciences*. 49: 119–135.
- Galvão, L.S., R. Almeida-Filho, and Í. Vitorello, 2005. Spectral discrimination of hydrothermally altered materials using ASTER short-wave infrared bands: Evaluation in a tropical savannah environment: *International Journal of Applied Earth Observation and Geoinformation*, 7(2):107-114.
- Goetz, A.F.H., B.N. Rock, and L.C. Rowan, 1983. Remote sensing for exploration: an overview. *Econ. Geol.* 78: 573–590.
- Gupta, R.P., 2003. *Remote Sensing Geology*, 2nd edition ed. Heidelberg, Springer, Berlin, 655.
- Harsanyi, J.C., Farrand, W.H., Chang, C.I., 1994. Detection of subpixel signatures in hyperspectral image sequences. *Proceedings of 1994 ASPRS Annual Conference*, Reno, Nevada. 236–247.
- Hassan, S.M., M.F. Sadek, and R.O. Greiling, 2014. Spectral analyses of basement rocks in El-Sibai-Umm Shaddad area, Central Eastern Desert, Egypt using ASTER thermal infrared data. *Arabian Journal of Geosciences*. 8: 6853-6865.
- Hegazi, A.M., and Z. Hamimi, 2002. Brittle tectonic Evolution of El Sibai-Abu El-Tiyur area, central Eastern Desert, Egypt. 6<sup>th</sup> international Conference on the Geology of the Arab World, Cairo University, 245-256.

- Hewson, R.D., T.J. Cudahy, S. Mizuhiko, K. Ueda, and A.J. Mauger, 2005. Seamless geological map generation using ASTER in the Broken Hill–Curnamona province of Australia. *Remote Sens. Environ.* 99: 159–172.
- Hunt, G.R., and P. Ashley, 1979. Spectra of altered rocks in the visible and near infrared: *Ecol. Geol.* 74: 1613-1629.
- Iwasaki, A., and H. Tonooka, 2005. Validation of a crosstalk correction algorithm for ASTER/SWIR: *IEEE Transactions on Geoscience and Remote Sensing*.43 (12): 2747-2751.
- Jensen, J.R., 2005. *Introductory Digital Image Processing*. Person Prentice Hall, Upper Saddle River.316.
- Kaufmann, H., 1988. Mineral exploration along the Aqaba–Levent structure by use of Landsat TM data: concepts, processing, and results. *Int. J. Remote Sens.* 9: 1639–1658.
- Kusky, T.M., and M. Matsah, 2003. Neoproterozoic dextral faulting on the Najd fault system, Saudi Arabia, preceded sinistral faulting and escape tectonics related to closure of the Mozambique Ocean. *Journal of the Geologic Society, London, Special issue on “Proterozoic East Gondwana: Supercontinent Assembly and Break-up”*, edited by M. Yoshida, B.F. Windley, S. Dasgupta, and C. Powell. 327–361.
- Mars, J. C., and L.C. Rowan, 2010. Spectral assessment of new ASTER SWIR surface reflectance data products for spectroscopic mapping of rocks and minerals: *Remote Sensing of Environment*. 114(9): 2011-2025.
- Meky, H.S.S., 1997. Geological, petrographical and geochemical studies on granitic rocks of Abu-El-Tiyur and Humrat Ghannam plutons, Eastern Desert, Egypt. Ph.D. Thesis, Al-Azhar Univ.
- Mohamed, M.A., 2001. Geology, petrology and radioactivity of Gabal El-Sebai area, Central Eastern Desert, Egypt. Ph.D. Thesis, Fac. Sci., Cairo Univ., Egypt.
- Ragab, A.I., B.A. El-Kalioubi, and Z. El-Alfy, 1993. Petrotectonic assemblages and crustal evolution of the area north of Abu El-Tiyur, Central Eastern Desert, Egypt, M.E.R.C. Ain Shams Univ., *Earth Sci. Ser.* 7: 1-16.
- Research Systems, Inc., 2008. ENVI Tutorials. Research Systems, Inc, Boulder, CO.
- Rogers, J.J.W., and J.S.S. Adams, 1969. Uranium. In: Wedepohl, K. H. (ed.) *Handbook of geochemistry*, New York, Springer-Verlag. 4: 92 B1- 92 C10.
- Rowan, L.C., A.F.H. Geotz, and R.P. Ashley, 1977. Discrimination of hydrothermally altered and unaltered rocks in visible and near infrared multispectral images. *Geophysics.* 42: 522-535.
- Rowan, L.C., S.J. Hook, M.J. Abrams, and J.C. Mars, 2003. Mapping hydrothermally altered rocks at Cuprite, Nevada, using the Advanced Spaceborne Thermal Emission and Reflection Radiometer (ASTER), a new satellite-imaging system. *Econ. Geol.* 98(5): 1019–1027.
- Rowan, L.C., J.C. Mars, and C.J. Simpson, 2005. Lithologic mapping of the Mordor N.T, Australia ultramafic complex by using the Advanced Spaceborne Thermal Emission and Reflection Radiometer (ASTER). *Remote Sens. Environ.* 99: 105– 126.
- Sabet, A.H., 1961. Geology and mineral deposits of Gebel El-Sebai area, Red Sea Hills, Egypt. Ph.D. Thesis, Leiden State Univ., The Netherlands.
- Salman, A.B., I.E. El-Aassy, and M.H. Shalaby, 1990. New occurrence of uranium mineralization in Gabal Gattar, northern Eastern Desert, Egypt. *Ann. Geol. Surv. Egypt.*16: 31-34.
- Stern, R.J., 1979. Late Precambrian ensimatic volcanic rocks in Central Eastern Desert of Egypt. Ph.D. Thesis, San Diego Univ. of California.
- Stern, R.J., 1994. Arc assembly and continental collision in the Neoproterozoic East African Orogen: implications for the consolidation of Gondwanaland. *Annual Review of Earth and Planetary Sciences.* 22, 319-351.
- Stern, R.J., and C.E. Hedge, 1985. Geochronologic and isotopic constraints on late Precambrian crustal evolution in the Eastern Desert of Egypt. *Am. J. Sci.* 285: 97–127.
- Streckeisen, A., 1976. To each plutonic its proper name. *Earth Sci. Rev.*, 12: 1-33.
- Sultan, M., R.E. Arvidson, and N.C. Sturchio, 1986. Mapping of serpentinites in the Eastern Desert of Egypt using Landsat Thematic Mapper data. *Geology.* 14: 995–999.
- Thome, K., F. Palluconi, T. Takashima, and K. Masuda, 1998. Atmospheric correction of ASTER. *IEEE Trans. Geosci. Remote Sens.* 36 (4): 1119–1211.
- Vincent, R.K., 1997. *Fundamentals of Geological and Environmental Remote Sensing*: Upper Saddle River, NJ: Prentice-Hall, Inc.